

TEST RESULTS ON PLASMA DIRECT CONVERTERS

ENERGY STORAGE,
SWITCHING, AND CONVERSION

WILLIAM L. BARR and RALPH W. MOIR
*University of California, Lawrence Livermore National Laboratory
P.O. Box 5511, Livermore, California 94550*

Received October 22, 1981

Accepted for Publication July 23, 1982

The power carried out through the ends of a mirror fusion reactor by escaping plasma can be converted directly into electricity by a plasma direct converter. Test results from three plasma direct converters are described. The first two tests were performed with a steady-state power density up to 70 W/cm² to simulate the predicted conditions on a reactor (~100 W/cm²). A single-stage unit and a two-stage unit of the venetian-blind type were tested up to 100 kV and 6 kW for a total time of ~80 h. In scaling up in energy from previous experiments, the new effects that became important were the ionization of background gas and the release of secondary electrons at surfaces. In the third test, a single-stage unit was mounted on the end wall of the Tandem Mirror Experiment (TMX) device where it intercepted some of the end-loss plasma. Of the 138 W incident on the direct converter, 79 W were recovered and 12 W were used to power the suppressor grid. The net efficiency was therefore 48%; this was in good agreement with predictions for a single-stage unit and the TMX plasma parameters.

These test results lend confidence to our direct-converter designs for fusion reactors. The remaining area of concern includes the general problem imposed by high-voltage breakdown in a large direct converter with many joules of stored energy.

I. INTRODUCTION

Plasma direct converters (PDCs) are designed to recover electrical power from the end-loss plasma in a mirror-type fusion reactor. They will necessarily be very large devices (occupying hundreds of square metres), and should be distinguished from beam di-

rect converters (BDCs), which recover power from the unneutralized ions in neutral beam injectors.

Work on PDCs began at Lawrence Livermore National Laboratory (LLNL) in 1970, soon after Post¹ first proposed a periodic, focusing type of PDC to improve the efficiency of mirror machines. Since then, testing² has been expanded from a 1-mW, 300-eV level to the 6-kW, 100-keV tests reported here. While the power level was being increased, the PDC concepts were simplified from the original 22-stage device to a single-stage device and a two-stage venetian-blind³ device. Recent experimental results with BDC are reported in Ref. 4. Typical efficiencies predicted for PDCs on tandem mirror reactors are 50% for a single-stage unit and 60% for a two-stage venetian-blind unit. These efficiencies can be realized with only one or two stages because the end-loss ions from the new tandem mirror⁵ devices have a high average energy and a narrow spread in energy.

The purpose of the present experiments is to test our predictions of PDC performance in reactor-like conditions. For that reason, the tests done on the test stand were performed at high voltage (up to 100 kV), in variable vacuum (10⁻² to 10⁻⁵ Pa), and in steady-state operation.

II. THE 100-keV TEST STAND

The test stand consists of a high-energy ion source, a magnetic lens, a drift space, and a chamber containing the PDC collectors. A photograph of the test stand is shown in Fig. 1. The ion source is a commercially available⁴ duoplasmatron. It produces a beam of up to 100 mA of hydrogen ions at up to 100 keV in steady-state operation. A lens magnet

⁴Our ion source was manufactured by General Ionex Corporation, Newburyport, Massachusetts.



Fig. 1. The test stand for testing PDCs in reactor-like conditions. The steady-state, 100-keV ion source is shown on the right.

0.5 m from the source controls the size of the beam at the location of the PDC, 3 m from the lens. By controlling the beam size, the lens allows the power density at the PDC to be varied up to $\sim 100 \text{ W/cm}^2$, the predicted limit³ (without emission of thermionic electrons) for radiatively cooled grid wires in a PDC as noted later.

The vacuum chamber is rather large (1.2 m in diameter) to allow room for the high-voltage feed-throughs, insulators, and the PDC structures. A base pressure of $1 \times 10^{-5} \text{ Pa}$ and an operating pressure of $3 \times 10^{-3} \text{ Pa}$ (uncorrected ion gauge readings) is maintained by two turbomolecular pumps. The true pressure in the hydrogen atmosphere is ~ 2.4 times the gauge reading. The addition of a 0.25-m-diam cryo-pump reduced these pressures by about an order of magnitude. The entire vacuum tank was covered with 2.5 mm of lead and the viewing ports were covered with lead glass to reduce the x-ray intensity below 0.2 mR/h everywhere outside the tank.

Diagnostics consist almost entirely of measurements of the electric currents and voltages at each electrode. For that reason, separate leads are brought

out from the grid wires and from the grid support structures. The heat generated at the final ion collector is also monitored. Since the operation is in steady state, data can be recorded on an x, y, y recorder, usually with the voltage of an ion collector as abscissa. Signals from current shunts at high voltage are telemetered out to the recorder. A variable resistor, consisting of a column of low-conductivity water, is used to vary the collector voltages.

III. THE SINGLE-STAGE DIRECTOR CONVERTER

The single-stage PDC consists of two grids followed by the ion collector as shown in Fig. 2. The first grid is grounded to shield the incoming plasma from the electric fields inside the PDC. The second grid is the electron suppressor, and is held sufficiently negative to repel the primary electrons. In the test stand, both the electron temperature and density are low at the grounded grid ($\sim 10 \text{ eV}$, $\sim 2 \times 10^7 \text{ cm}^{-3}$), giving a Debye shielding length of $\sim 5 \text{ mm}$. Wires with spacings of 2 cm in the grounded grid can therefore

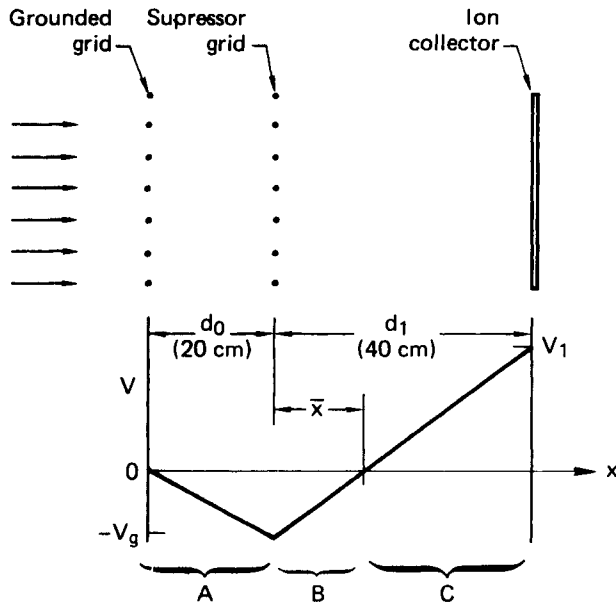


Fig. 2. The geometry and potential in a single-stage direct converter. Cold plasma produced in regions A, B, and C results in losses.

define the potential to within a few tens of volts in the grid plane.

Each grid is made of spring-tensioned tungsten wires, 1 mm in diameter and spaced 20 mm between centers. The grid frames are shielded to prevent them from collecting current. As shown in Fig. 2, the spacing d_0 between grid planes is 20 cm while the spacing d_1 between suppressor grid and ion collector is 40 cm. This value for d_1 was determined by the maximum space charge expected without the formation of a virtual anode.³ A virtual anode should be avoided because it would cause the ions to move with low energy and a large cross section for charge exchange (see Sec. IV).

When the incident electrons are cold relative to possible acceleration energies (as they are in the test stand), the situation at the suppressor grid is the same as at the control grid in a plane triode vacuum tube when it is operated at cutoff. The required ratio of grid voltage-to-plate voltage for that case has been calculated⁶ as a function of grid geometry. In the test stand, we find (both analytically and experimentally) that -3 kV is required at the suppressor grid when the ion collector is at $+100$ kV.

To avoid the danger of sparking, all electric fields should be kept well below 100 kV/cm. The maximum electric field at the surface of a grid wire is difficult to calculate, but the average field is (from Gauss' law) (a Nomenclature appears on p. 110):

$$\bar{E}_r = \frac{a}{2\pi r} (E_1 + E_2) ,$$

where

a = wire spacing

$2r$ = wire diameter

E_1 and E_2 = magnitudes of the electric fields far out on either side of the grid plane.

Here, the grid opacity $2r/a = 0.05$, $E_1 \approx 0$ (the cutoff condition), and $E_2 \approx 3.4$ kV/cm. (This maximum E_2 allows for space charge.) In this case, the average electric field on the surface of a wire in the suppressor grid is $E_r \approx 22$ kV/cm and the maximum is slightly greater. No sparking has been detected at the wires.

Tungsten was chosen for the grid-wire material because its large work function (4.52 eV) allows a high operating temperature without emission of thermionic electrons. At a temperature of ~ 1900 K, tungsten should give an emission current equal to the intercepted ion current. This condition is taken as the temperature limit for the suppressor grid and sets the power density limit of ~ 100 W/cm² for a PDC.

The ion collector in the single-stage PDC is also used as the second collector in the two-stage PDC. It is a water-cooled copper disk with the central section isolated both electrically and thermally. This allows calorimetry with fast enough response to follow the changes in heat as the voltage is scanned. The outer edge of the collector is rolled in (as shown in Fig. 3) to provide a smooth outer surface for voltage holding and to approximate Pierce electrodes to prevent the space-charge blowup of the beam where its velocity is low and density high. Figure 3 shows the single-stage PDC mounted in the collector tank. The vacuum feedthrough for the ion collector consists of a 380-mm-long, 200-mm-i.d. ceramic pipe with O-ring seals on the ends, through which a 63-mm-diam stainless steel tube passes coaxially. A tube this size minimizes the radial electric field inside the feedthrough (giving $E < 32$ kV/cm) and provides a smooth shroud around the water lines. The weight of the collector is supported by an insulator resting on the bottom of the vacuum tank behind the collector (as shown later for the two-stage PDC). When the second collector stage was added, similar feedthroughs and supports were used there also.

IV. LOSSES IN A SINGLE-STAGE PDC

The efficiency of the PDC is reduced by any process that either prevents primary ions from depositing their charge on the collector or that allows electrons to reach the collector. Efficiency is also reduced by any process that causes a current drain in the negative grid circuit. Loss processes can be classified according to whether or not they involve the interaction of the background gas. When a primary

ion either ionizes or undergoes charge exchange with a gas molecule, the result to the PDC depends on where the interaction takes place. The inside of a single-stage PDC divides naturally into three regions as indicated in Fig. 2. Regions A and B form a

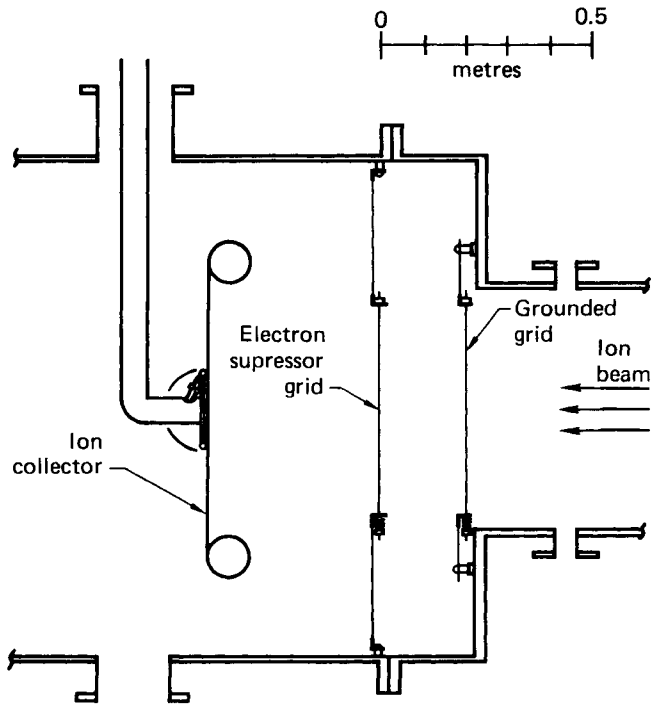


Fig. 3. Top view of the single-stage direct converter installed in the test stand. The water-cooled ion collector is made of copper. The grids are made of individually, spring-tensioned 1-mm tungsten wires.

potential well where cold ions can be trapped, while region C is positive and contains a strong electric field that decelerates the primary ions and expels cold ions.

In evaluating these effects, we assume that the gas density and the opacity of the grids are small enough that we can ignore second-order effects. For example, we ignore the interception of reaction products on the grids.

In Table I the contributions to the suppressor grid current I_g , and to the net positive current to the collector I_1 are itemized. In the table, both σ_{cx} (the cross section for charge exchange of a beam ion with a gas molecule) and σ_i (the cross section for the production of electrons by the collision of beam ions with gas molecules) are assumed to be constant in regions A + B, but not in C. To allow for variations in region C, $S_{cx}(\bar{x}, d_1)$ is defined as:

$$S_{cx}(\bar{x}, d_1) = \int_{\bar{x}}^{d_1} \sigma_{cx} dx = \frac{d_1}{V_g + V_1} \int_{W-V_1}^W \sigma_{cx} dW,$$

and $S_i(\bar{x}, d_1)$ is defined similarly. Here W is the initial ion energy in electron volts, and V_g and V_1 are the magnitudes of the grid and collector voltages, respectively. The distances \bar{x} and d_1 are defined in Fig. 2. Since this is a small correction term, it is permissible to use the vacuum potential in calculating \bar{x} .

Other quantities that appear in the table are: I , the incident ion beam current; T_g , the transparency of each grid; n_0 , the gas density; γ_1 and γ_c , the coefficients for the production of secondary electrons at surfaces by primary ions and by cold ions, respectively. The coefficient r^+ for the electrostatic reflection of an ion back from a metal surface is taken as $r^+ = \exp[-(W - V_1)^2/D^2]$ if $W > V_1$, and $r^+ = 1$

TABLE I

Net Current I_1 to the Ion Collector and the Grid Current I_g as Fractions of the Incident Ion Current I^*

Process/ Region	I_g/I	I_1/I
cx/A^a	$T_g n_0 \sigma_{cx} d_0 (1 + \gamma_c) B_1$	$-T_g n_0 \sigma_{cx} d_0 (A_1 + f \gamma_c)$
i/A	$T_g n_0 \sigma_i d_0 (1 + \gamma_c) B_1$	$-T_g n_0 \sigma_i d_0 f \gamma_c$
cx/B^a	$T_g^2 n_0 \sigma_{cx} \bar{x} (1 + \gamma_c) B_1$	$-T_g^2 n_0 \sigma_{cx} \bar{x} (B_1 + f \gamma_c)$
i/B	$T_g^2 n_0 \sigma_i \bar{x} (1 + \gamma_c) B_1$	$-T_g^2 n_0 \sigma_i \bar{x} (A_1 + f \gamma_c)$
cx/C^a		$-T_g^2 n_0 S_{cx}(\bar{x}, d_1) A_1$
i/C		$-T_g^2 n_0 S_i(\bar{x}, d_1) A_1$
$T_g/sup.$	$T_g O_g (1 + \gamma_1) (1 + T_g r^+)$	$T_g^2 A_1 - T_g O_g \gamma_1 (f^{-\frac{1}{2}} + T_g r^+)$
$r^0/1$	$T_g^2 r^0 O_g \gamma_c A_1$	$-T_g^2 r^0 O_g \gamma_c A_1$

*The symbols are defined in the text except for: $O_g = 1 - T_g$, $A_1 = 1 - r^+$, and $B_1 = 1 + r^+$.

^aSee Fig. 2 for regions A, B, and C.

otherwise as would result from a Gaussian distribution of ion energy. The data indicate that $D = 2$ keV, apparently due to scattering by the grids. Similarly, r^0 is the coefficient for the reflection of the ion back from a surface as a fast neutral atom, and has a maximum value⁷ of ~ 0.4 . The significance of r^0 in a PDC is due to the secondary electrons released by the fast atoms. An expression for the product ($r^0\gamma_c$) that is compatible with published values of both r^0 and γ_c and with our data is:

$$(r^0\gamma_c) = 0.002\gamma_c(W - V_1) \ln [65/(W - V_1)] ,$$

if $0 < W - V_1 < 65$, or ($r^0\gamma_c$) = 0 otherwise. The γ_c appearing on the right side is treated as a parameter, and W and V_1 are measured in kiloelectron volts.

The quantity f gives the fraction of the secondary electrons, released from the suppressor grid, that reach the ion collector when the grid is bombarded from both sides. To evaluate f , we calculated electron trajectories starting from different regions on a wire. Because the angular dependence of the bombardment effectively cancels the angular dependence of the emission coefficient γ , the emission of secondary electrons is nearly uniform over the surface of a wire. An approximate fit to the results of the numerical calculation is:

$$f = 1 - \frac{1}{2} \exp(-V_1/10V_g) .$$

By adding the currents that are itemized in Table I, we obtain the total current I_g in the suppressor grid circuit, and the net current from the ion collector I_1 . The result is

$$I_g = IT_g n_0 (\sigma_{cx} + \sigma_i) (d_0 + T_g \bar{x}) (1 + \gamma_c) (1 + r^+) + IT_g (1 - T_g) [(1 + T_g r^+) (1 + \gamma_1) + T_g r^0 \gamma_c] \quad (1)$$

and

$$I_1 = IT_g^2 - IT_g n_0 [(\sigma_{cx} + \sigma_i) (d_0 + T_g \bar{x}) (1 + f\gamma_c) - \gamma_i d_0 + S_{cx}(\bar{x}, d_1) T_g + T_g S_i(d_1, \bar{x})] - \left\{ IT_g (1 - T_g) \times \left[1 + \left(f - \frac{1}{2} \right) \gamma_1 + T_g r^+ \gamma_1 + T_g r^0 \gamma_c \right] + IT_g^2 r^+ \right\} \quad (2)$$

where

$$\bar{x} = \frac{V_g d_1}{V_g + V_1}$$

is the thickness of region B. When the gas density n_0 is large, region B makes the dominant contribution to I_g for small values of V_1 (where $\bar{x} \approx d_1 = 2d_0$). Experimentally, we observe the decrease in I_g due to \bar{x} as V is increased from zero. The predictions of Eqs. (1) and (2) are compared with observations in Sec. V.

Using these expressions for the currents, we can predict the net efficiency η of power recovery by the single-stage PDC as a function of collector voltage V_1 :

$$\eta = \frac{I_1 V_1 - I_g V_g}{IW} , \quad (3)$$

where W is the energy of the incident ions. If there is a significant spread in the energy of the ions arriving at the PDC, each term in Eqs. (1) and (2) must be averaged over the energy distribution. The denominator in Eq. (3) becomes the total incident power, including the power from the electrons. In recent analyses⁸ of tandem mirror reactors, the electron power is typically $\sim 10\%$ of the ion power.

V. TEST RESULTS WITH THE SINGLE-STAGE PDC

The electrical circuit used with the single-stage PDC is shown in Fig. 4. A power supply maintains the negative voltage $-V_g$ at both the suppressor grid and its support. The currents from the grid and its support pass through separate shunts for monitoring. The output from the shunts is telemetered out to the recorder. The positive voltage V_1 at the ion collector is developed by the collector current I_1 flowing through the load resistor R . A voltage divider provides an output proportional to V_1 , while I_1 is measured by the shunt at the low-voltage end of R . An x, y, y recorder records I_1 and I_g as a function of V_1 , which changes as R is varied.

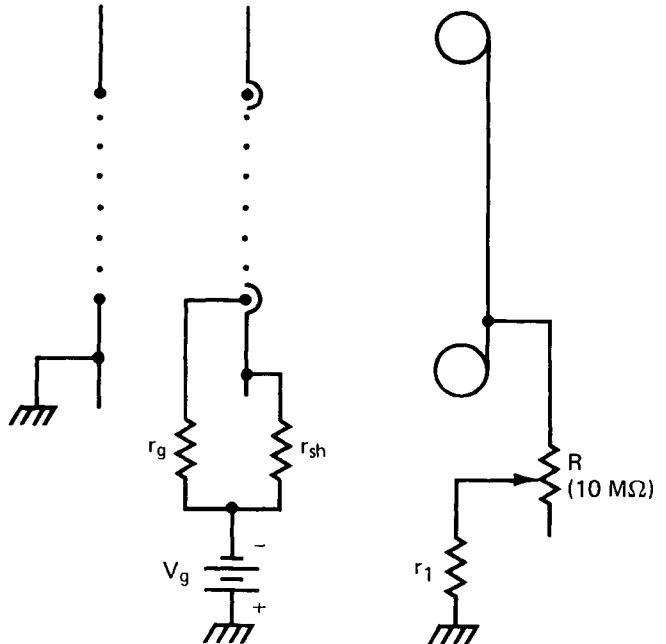


Fig. 4. Single-stage direct converter electrical circuit. The collector voltage V_1 is developed across the variable 10-M Ω load resistor.

Figure 5 shows a set of data taken when the gas pressure $p = 2.9$ mPa (2.2×10^{-5} Torr uncorrected ion gauge reading) and $V_g = 3$ kV. The currents due to ions at one-third, one-half, and two-thirds of full energy can be seen. These ions result from full-energy H_2^+ and H_3^+ ions in the beam, some of which collide with gas molecules and break up before reaching the PDC. These and other features of the data are reproduced in the calculated currents, plotted as dashed curves in the figure. The decrease in I_g at low values of V_1 is due to the decrease in \bar{x} , as discussed earlier. The break in both I_g and I_1 as V_1 approaches W , the beam energy, is due to the reflection of ions and the resulting increase in secondary electron current.

Figure 6 shows a set of data and the calculated currents when $p = 5.7$ mPa (4.3×10^{-5} Torr, gauge reading), about twice that in Fig. 5. The effects of changes in p are easily seen by comparing the two figures, and are reproduced by the calculations. More of the molecular ions break up and form fractional energy ions when the pressure is raised. The agreement between theory and experiment is apparently limited only by the uncertainties in the parameters and their dependence on energy.

Because a PDC will have to operate in a magnetic field of perhaps 0.01 T, a test was conducted to detect any unpredicted effects. The application of a 0.006-T magnetic field, directed along the beam direction, had no detectable effect on the PDC data after a short period of outgassing that initially caused voltage breakdown.

VI. STRUCTURE OF THE VENETIAN-BLIND COLLECTOR STAGE

The two-stage PDC was made by modifying the single-stage unit. All electrodes were tilted as required by the venetian-blind concept,³ and the intermediate collector structure was inserted between the negative grid and the solid collector. The tilt angle was set at 7.5 deg and each of the three major electrode spacings (d_0 , d_1 , and d_2) was set at 20 cm to allow either ion collector to be varied over the full range from 0 to 100 kV.

The venetian-blind structure is contained inside a smooth frame formed from 25-mm-diam stainless steel tubing as shown schematically in Fig. 7. Each of the molybdenum ribbons passes through a guide slot at each end and is tensioned by a coil spring to maintain alignment. The ribbons are 0.13 mm thick, 66 mm wide, and are spaced 20 mm apart. Located 25 mm behind each ribbon is a 0.25-mm wire forming a grid whose purpose is to return the secondary electrons to the ribbons. Since the potential of this grid is only a few kilovolts lower than that of the ribbons, it is supported by low-voltage insulators mounted on the ribbon frame.

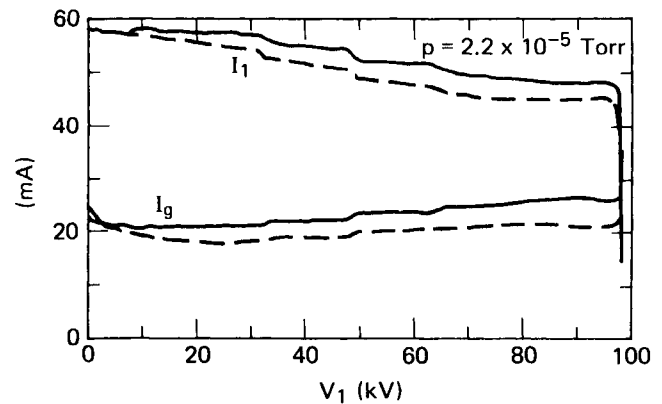


Fig. 5. Data from the single-stage PDC taken in good vacuum (2.9 mPa). Collector current I_1 and grid current I_g are recorded as a function of collector voltage V_1 . The dashed curves are calculated currents. Notice the steps at 33, 50, and 67 kV where fractional energy ions are turned back.

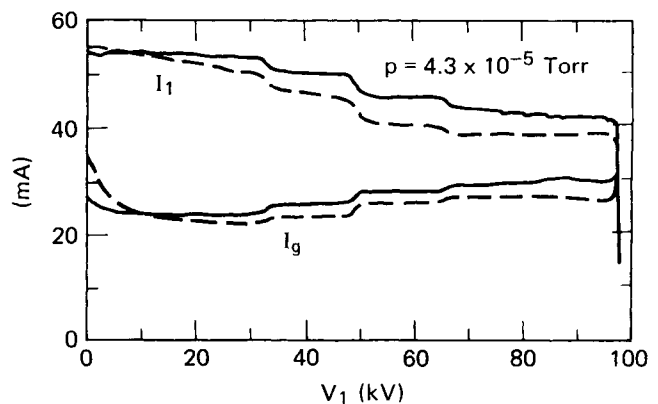


Fig. 6. Data taken at higher pressure (5.7 mPa) for comparison with Fig. 5. The increased ionization and charge exchange at this higher pressure caused increased loss currents. The calculated currents at this pressure are shown by the dashed curves.

VII. LOSSES IN A TWO-STAGE PDC

The purpose of the intermediate collector stage in a two-stage PDC is to recover those ions that are electrically reflected from the high-potential stage. The ribbons in the venetian-blind structure are designed to pass fast ions moving at the proper angle in the forward direction and to block any reflected fast ions at the reverse angle. However, the electrons and ions that are created inside the PDC start with low initial energy and therefore follow trajectories that are nearly straight and normal to the planes of the electrodes. For these particles, the ribbon structure has a geometrical transparency, T_r , of $\sim 40\%$.

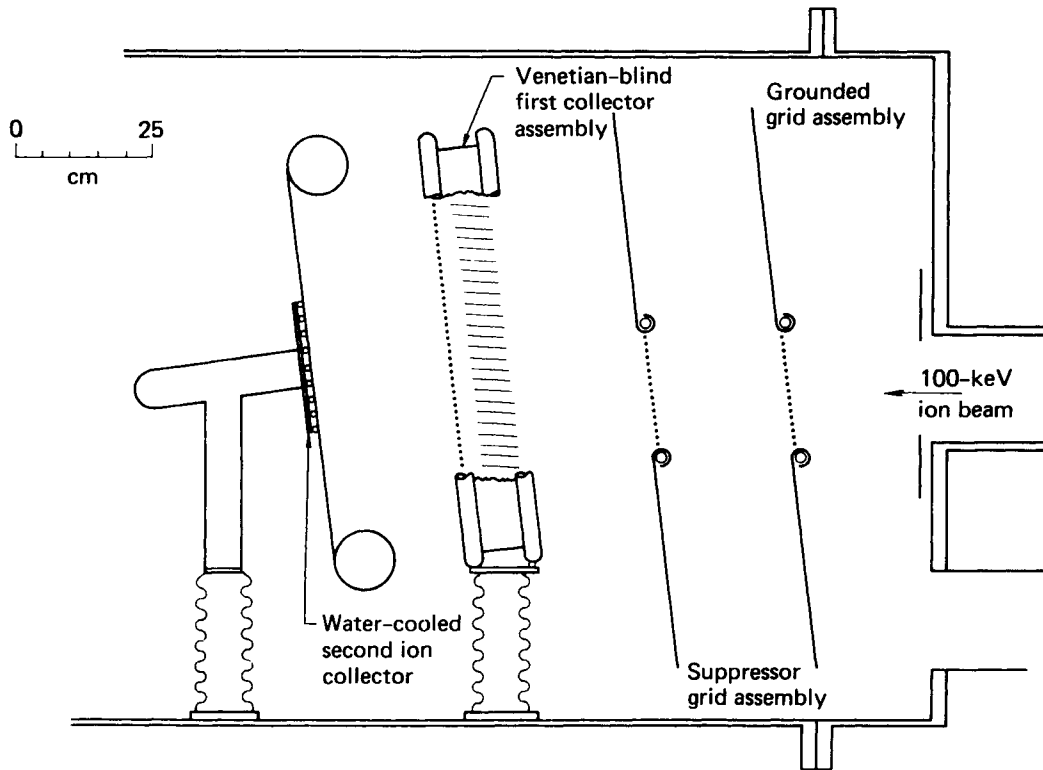


Fig. 7. Side view of the two-stage PDC installed in the test stand. The venetian-blind, intermediate collector is made of spring-tensioned molybdenum ribbons. The second collector and grids are as shown in Fig. 3.

Therefore, ~60% of the loss current is caught on the intermediate stage and prevented from falling through an even larger potential difference.

A suppressor grid held less positive than the venetian-blind structure follows it and prevents that structure from becoming a source of secondary electrons. Calculations showed the bias voltage $V_1 - V_{rg}$ should be 5 kV to allow V_2 to exceed V_1 by 100 kV. Experimentally, we observe that a 3-kV bias allows a significant electron current to flow.

The inside of a two-stage PDC divides naturally into four regions as indicated in Fig. 8. Regions A and B (as in a single-stage unit) form a potential well for cold ions that must finally be collected on the suppressor grid. Cold ions formed in region C are expelled from the PDC, and we ignore the few that are intercepted by grid wires. Cold ions formed in region D must pass through the ribbons to escape. A fraction T_r escape while the remaining $1 - T_r$ are caught on the ribbons. Electrons produced in region A are expelled, while those from regions B and C are attracted toward the ribbons. A fraction $1 - T_r$ strike ribbons and the other T_r pass through and reach the second ion collector. All electrons produced in region D go to the second collector.

In general, the addition of the intermediate collector stage divides the loss currents and reduces the

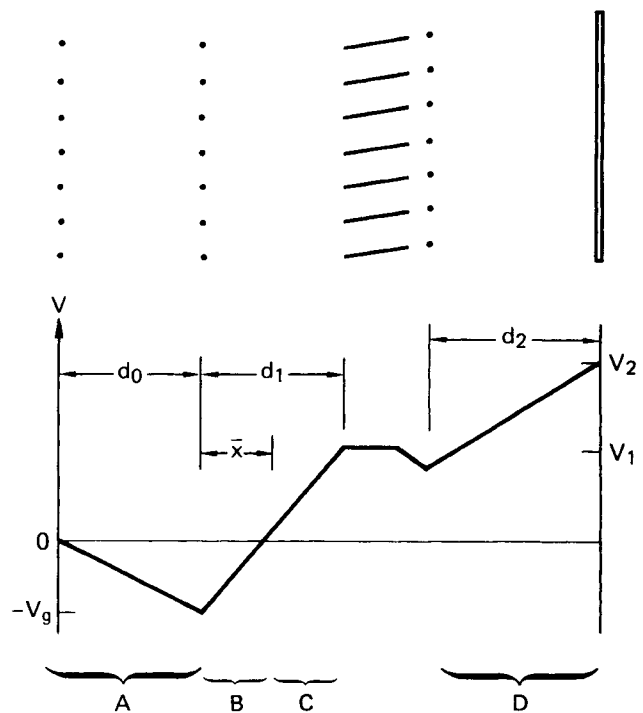


Fig. 8. The potential distribution and regions used in calculating the loss currents in a two-stage PDC.

power consumed by them. However, some power is lost when fast ions that could have reached the second, higher voltage stage are intercepted by the ribbons. For ribbons of negligible thickness, the intercepted fraction,³ $1 - T_f$, of primary ions of energy W is

$$1 - T_f = \frac{l}{h} \left| \sin \alpha_1 - \frac{\cos \alpha_1 \sin \alpha_0}{\left(\cos^2 \alpha_0 - \frac{V_1}{W}\right)^{1/2}} \right| .$$

Here, $\alpha_0 = 7.5$ deg is the incident angle at the first grid, $\alpha_1 = 10.5$ deg is the slope angle of the ribbons of width l and separation h .

Table II lists the contributions to I_g , the suppressor grid current; to I_{rg} , the ribbon suppressor grid current; and to I_1 and I_2 , the positive currents from the first and second ion collector, respectively. The other new quantities are:

$$S_{cx}(d_1, d_2) = \int_{d_1}^{d_2} \sigma_{cx} dx = \frac{d_2}{V_2 - V_1} \int_{W-V_2}^{W-V_1} \sigma_{cx} dW ,$$

and similarly for $S_i(d_1, d_2)$. The reflection coefficient r_2^+ (for ions at the second collector) is found experimentally to have a significant value even when $W > V_2$, apparently because of scattering as the beam passes through the ribbons. To reproduce the data we use

$$r_2^+ = 0.35 [1 - (1 - V_2/W)^{1/2}] (V_2/W) ,$$

if $W > V_2$ and $r_2^+ = 1$ otherwise. The subscript 1 indicates that the reflection takes place at the ribbons and is a function of $W - V_1$, while subscript 2 means that the dependence is on $W - V_2$.

The expression for the efficiency of a two-stage PDC, corresponding to Eq. (3) for a single-stage unit, is:

$$\eta = \frac{I_1 V_1 + I_2 V_2 + I_{rg} V_{rg} - I_g V_g}{IW} . \quad (4)$$

Of course, a two-stage PDC should only be used if the ions have a spread in energy. In that case, each of the currents (I_1 , I_2 , I_{rg} , and I_g) must be averaged over the ion energy distribution, and the denominator in Eq. (4) replaced by the total incident power—including any incident electron power.

VIII. RESULTS WITH THE TWO-STAGE PDC

Because we use a monoenergetic beam, there are two modes in which the two-stage PDC can operate. Either $W > V_2$, in which case most of the beam ions reach the second stage, or $W < V_2$, and the beam ions are turned back to the first stage. (In our previous PDC tests at low power and low voltage, we used a power supply connected in parallel with the PDC across a load resistor. That allowed the scanning of V_2 from 0 to above W .) In the first case, we use the circuit shown in Fig. 9 and allow the collectors to

TABLE II.a
Net Current I_1 to the Ion Collector and Grid Current I_g as Fractions of the Incident Ion Current*

Region	$I_g/I T_g$	$I_1/I T_g$
A ^a	$n_0(\sigma_i + \sigma_{cx})d_0(1 + \gamma_c)B_1$	$-n_0d_0[\sigma_{cx}r_2^+A_1 + (\sigma_{cx} + \sigma_i)O_r\gamma_c(f + r_1^+)]$
B ^a	$T_g n_0(\sigma_i + \sigma_{cx})\bar{x}(1 + \gamma_c)B_1$	$-T_g n_0\bar{x}[\sigma_{cx}r_2^+A_1 + \sigma_i O_r B_1 + O_r(f + r_1^+)\gamma_c(\sigma_{cx} + \sigma_i)]$
C ^a		$-T_g n_0[r_2^+ S_{cx}(\bar{x}, d_1)A_1 + O_r S_i(\bar{x}, d_1)B_1]$
D ^a		$T_g n_0[(O_r - r_2^+)S_{cx}(d_1, d_2) + O_r S_i(d_1, d_2)B_2]A_1$
g	$O_g(1 + \gamma_1)B_1$	$-O_g[r_2^+ + (f - \frac{1}{2} + r_1^+)O_r\gamma_1]$
1 ^b	$T_g O_g r_1^0 r_2^+ \gamma_c T_f A_1$	$-T_g r_1^0 \gamma_c (O_g T_f O_r r_2^+ + O_{rg} O_f)A_1$
1 ^b		$T_g (O_f - O_{rg}\gamma_1 + T_f T_{rg} r_2^+)A_1$
2 ^b	$T_g T_f r_2^0 T_f O_g \gamma_c A_1$	$T_g T_f r_2^0 T_r O_g \gamma_c A_1$

*For brevity:

$$\begin{array}{llll} A_1 = 1 - r_1^+ & A_2 = 1 - r_2^+ & O_r = 1 - T_r & O_{rg} = 1 - T_{rg} \\ B_1 = 1 + r_1^+ & B_2 = 1 + r_2^+ & O_g = 1 - T_g & O_f = 1 - T_f \end{array}$$

^aSee Fig. 9 for regions A, B, C, and D.

^bRefer to collectors 1 and 2.

TABLE II.b

Net Current I_2 to the Ion Collector and Suppressor Grid Current I_{rg} as Fractions of the Incident Ion Current*

Region	I_{rg}/IT_g	I_2/I_g
A ^a		$-n_0d_0[\sigma_{cx}A_2A_1 + (\sigma_{cx} + \sigma_i)T_r\gamma_c(f + r_1^+)]$
B ^a		$-T_gn_0\bar{x}[\sigma_{cx}A_2A_1 + \sigma_iT_rB_1 + (\sigma_{cx} + \sigma_i)T_r\gamma_c(f + r_1^+)]$
C ^a		$-T_gn_0[B_2S_{cx}(\bar{x}, d_1)A_1 + T_rS_i(\bar{x}, d_1)B_1]$
D ^a		$-T_gn_0[A_2S_{cx}(d_1, d_2) + B_2S_i(d_1, d_2)]A_1$
g		$-O_g[A_2A_1 + (f - \frac{1}{2} + r_1^+)T_r\gamma_1]$
1 ^b	$T_g r_1^0 O_{rg} O_f A_1$	$-T_g r_1^0 O_g T_f \gamma_c T_r r_2^+ A_1$
1 ^b	$T_g O_{rg} (1 + T_f r_2^+) (1 + \gamma_1) A_1$	$T_g T_f (A_2 - O_{rg} r_2^+ \gamma_1) A_1$
2 ^b	$T_g T_f r_2^0 O_{rg} \gamma_c A_1$	$-T_g T_f r_2^0 O_{rg} \gamma_c A_1$

*For brevity:

$$\begin{aligned}
 A_1 &= 1 - r_1^+ & A_2 &= 1 - r_2^+ & O_r &= 1 - T_r & O_{rg} &= 1 - T_{rg} \\
 B_1 &= 1 + r_1^+ & B_2 &= 1 + r_2^+ & O_g &= 1 - T_g & O_f &= 1 - T_f
 \end{aligned}$$

^aSee Fig. 9 for regions A, B, C, and D.

^bRefer to collectors 1 and 2.

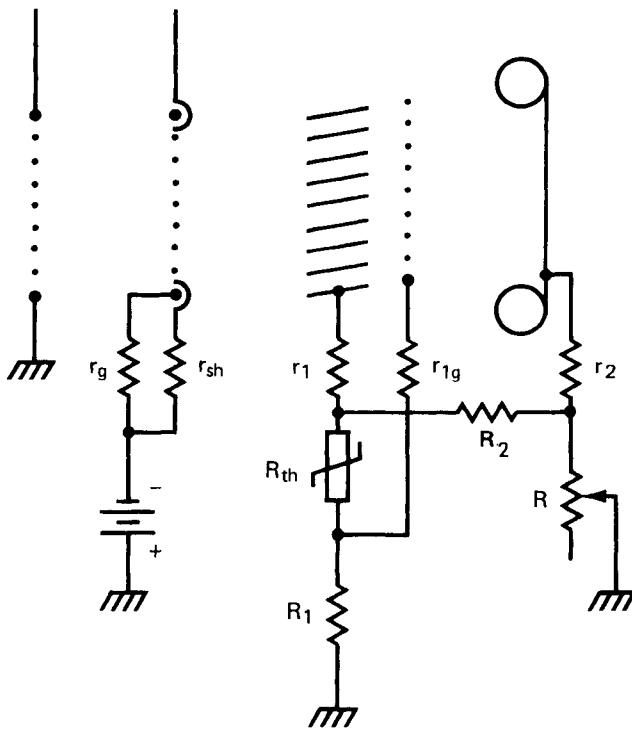


Fig. 9. The electrical circuit used to scan the collector voltages in the mode where V_2 is less than the beam energy. The voltage of the molybdenum ribbons is about half of V_2 , while the nonlinear resistor keeps the ribbon's suppressor grid another 4 to 5 kV lower.

self-bias, as is done with the single-stage unit. A variable resistor, R , is the control element. A nonlinear resistor, R_{th} , is used to maintain the ribbon suppressor grid ~ 5 kV less positive than the ribbons, even though the currents vary. We record the five currents through the shunts r_g , r_{sh} , etc., as functions of the two voltages, V_1 and V_2 , both of which vary with R . The five currents are: I_g , suppressor grid; I_{sh} , grid mount and shield; I_1 , ribbons; I_{rg} , ribbon suppressor grid; and I_2 , second collector.

A set of data taken with this circuit and at a beam energy of 80 keV and a pressure of 0.4 mPa (3×10^{-6} Torr, gauge) is shown in Fig. 10. Currents to the electrodes, and the voltage V_1 , are recorded as functions of V_2 . It is important that I_2 in Fig. 10 remains reasonably high almost up to $V_2 = W$, and that all important losses are explainable by the terms listed in Table II. The currents calculated from Table II are shown dashed. The change in the curves at about $V_2 = 4$ kV occurs where $V_2 > V_1$ begins and electrons instead of cold ions move toward the second collector. Notice that as V_2 approaches W and I_2 decreases sharply, I_1 starts to increase as it should. However, the sum $I_1 + I_2$ is not constant and the reason can be seen in Table II. The number of cold ions that result from ionization and charge exchange in region D increases as V_2 is increased, but only $1 - T_r$ of the ions and all of the electrons are caught. Also, f increases as V_1 increases.

It should be pointed out that the suppressor grid

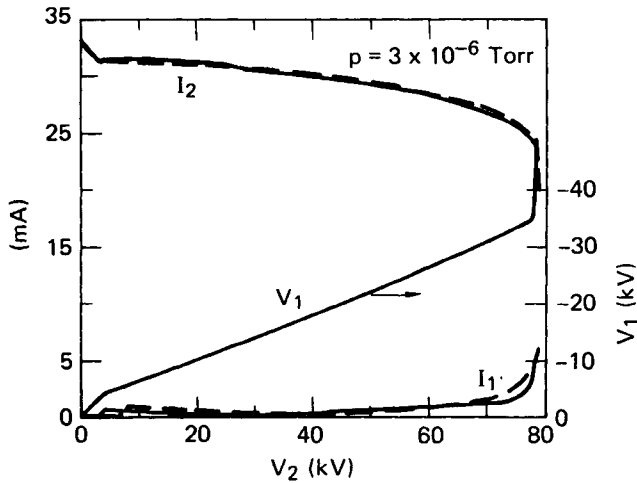


Fig. 10. Data from the two-stage PDC using the circuit shown in Fig. 9. In this mode of operation, most of the ions pass through the first collector and are collected at the second collector (I_2). The dashed curves show the predicted currents.

behind the ribbons is essential. When it is not biased sufficiently negative (>4 kV) relative to the ribbons, I_2 decreases rapidly to nearly zero as V_2 is increased while I_1 increases. This indicates a flow of electrons from the ribbons (I_1) to the second collector (I_2).

For operation in the second mode, where $V_2 > W$ and the ions are collected on the ribbons at V_1 , we use the circuit shown in Fig. 11. The second collector is connected directly to the acceleration power supply for the source. Because of a $25\text{-k}\Omega$ dropping resistor at the source, this results in $V_2 - W \approx 2$ kV. The first collector is self-biased as the net current that it collects flows through the nonlinear resistor and then the variable load resistor. By varying the load resistor, we scan V_1 through the design point $V_1 = W/2 \approx V_2/2$. The ribbons were designed to give a maximum forward transmission of primary ions when $V_1 = W/2$.

Figure 12 shows a set of data where I_1 , I_{rg} , and I_2 are recorded as functions of V_1 , while $V_2 = W + 1.6 = 100$ kV and $p = 0.53$ mPa (4×10^{-6} Torr, gauge). The general shape of the I_1 versus V_1 curve with its rather sharp shoulder near the high end agrees with the calculated curve (dashed). The value of I_2 is negative in this mode because it can collect no ions, and both I_2 and I_{rg} are larger than the calculated values. We are apparently underestimating the secondary electron emission from that grid.

The dip in I_1 at $V_1 \approx 60$ kV is due to an effect that we had not encountered in the low-energy tests. Collection of ions on the ribbons occurs at near-grazing incidence, which results in a large value⁷ of r^0 . The resulting neutral atoms are energetic enough

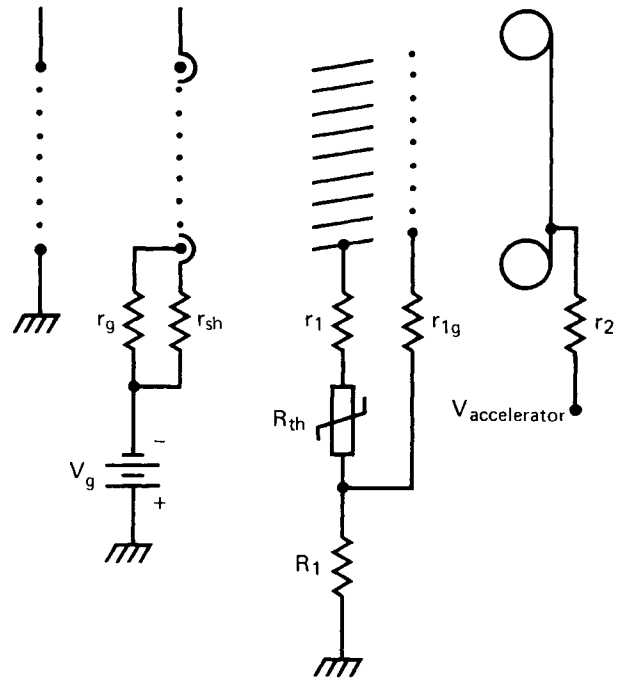


Fig. 11. The electrical circuit to produce a voltage at the second collector that is greater than the beam energy.

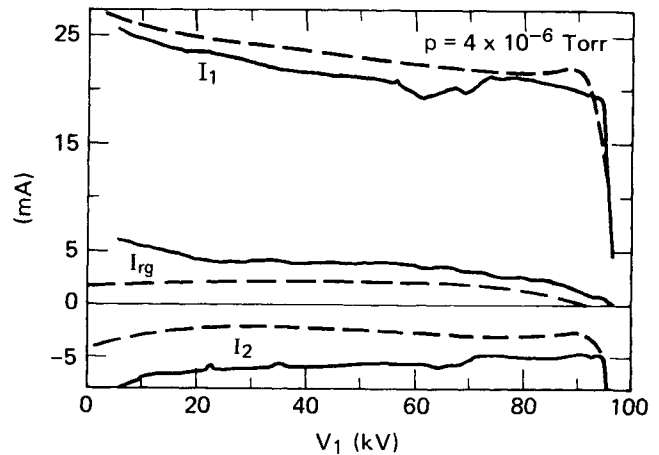


Fig. 12. Two-stage PDC data using the circuit shown in Fig. 11. In this mode, the ions are turned back and most of them are collected on the ribbons (I_1). Loss currents produce a negative I_2 . The dashed curves show the predicted currents.

to release secondary electrons from surfaces. On the test stand, the support frames for the grids can be struck, and they offer a large surface area that yields a large electron current. There appears to be a focusing of the neutrals onto the frame when $V_1 = 60$ to 70 kV. We tested this hypothesis by installing an

auxiliary suppressor grid over the suspected area of the grid frame. By biasing the new grid at least 300-V negative relative to the grid frame, we could almost eliminate the electron current. This is an effect that must be allowed for in future designs.

With the exception of the dip at $V_1 \approx 60$ kV, the agreement is satisfactory between the measured and predicted currents. In evaluating the terms in Table II, we assume $\gamma_1 = 3$, $\gamma_c = 2$, $T_g = 0.95$, and use cross sections from the published⁹ literature for H^+ and H_2^+ in H_2 gas. We use our calculated values for f , T_r , and T_f . The shape of the shoulder near maximum V_1 depends on the functional dependence of r_1^0 and r_1^+ on V_1 . We used the expression for r_1^+ described in the discussion of losses in the single-stage PDC, but we changed the expression for r_1^0 to account for the grazing angle of incidence on the ribbons. Since the angle depends on the ratio $y = V_1/W$, we used the expression $r_1^0 = 3.6y^4(1 - y^2)$ as an approximation to the combined angular and energy dependence of the reflection coefficient when $0 < y < 1$.

If there is a distribution of ion energies, the calculated currents can be averaged over the distribution to obtain the efficiency of a PDC in that case. Again, the denominator in Eq. (4) must include the total power carried by both ions and electrons incident on the PDC.

IX. A PDC TEST ON THE TANDEM MIRROR EXPERIMENT (TMX)

A single-stage PDC was tested on the end flux from the TMX device.¹⁰ This was the first test of a

PDC in which plasma generated for another purpose was used. The module had a 130-mm-diam entrance aperture and was mounted on the end wall where it intercepted a magnetic flux tube coming from 10 mm off axis in the end cell. Figure 13 shows the location on the TMX vacuum vessel. The grids were made with 0.05-mm tungsten wires with 1.5-mm spacings to operate where the Debye length is of the order of 1 mm. The density¹⁰ of fast ions at the end wall is 4×10^8 cm^{-3} and the temperature of the confined electrons is ~ 80 eV. Therefore, the Debye length could be as large as 3 mm. Recent probe measurements¹¹ indicate that the electron temperature near the end wall is ~ 5 eV, which gives a Debye length of ~ 0.7 mm. In the test of the PDC, it was found that ~ 500 V was required at the suppressor grid. This high value of grid voltage is consistent with either a high electron temperature (80 eV) or a short Debye length (~ 1 mm).

The PDC module is shown in Fig. 14. A string of zener diodes with taps at 102-V intervals was used as a load to generate the collector potential. The taps were changed between pulses of the TMX experiment. Therefore, a complete scan of the collector voltage required a series of nearly identical pulses. One such set of data is shown in Fig. 15. The collector current remained nearly constant at ~ 0.14 A until the collector voltage was increased above $V_1 = 565 \pm 20$ V. This is a measure of the minimum ion energy, and therefore of the ambipolar potential in the TMX end cells. The rate of decrease of current for $V_1 > 565$ V measures the energy distribution of those confined ions that scatter into the loss cone. If the loss cone is full in TMX, then the rate of decrease

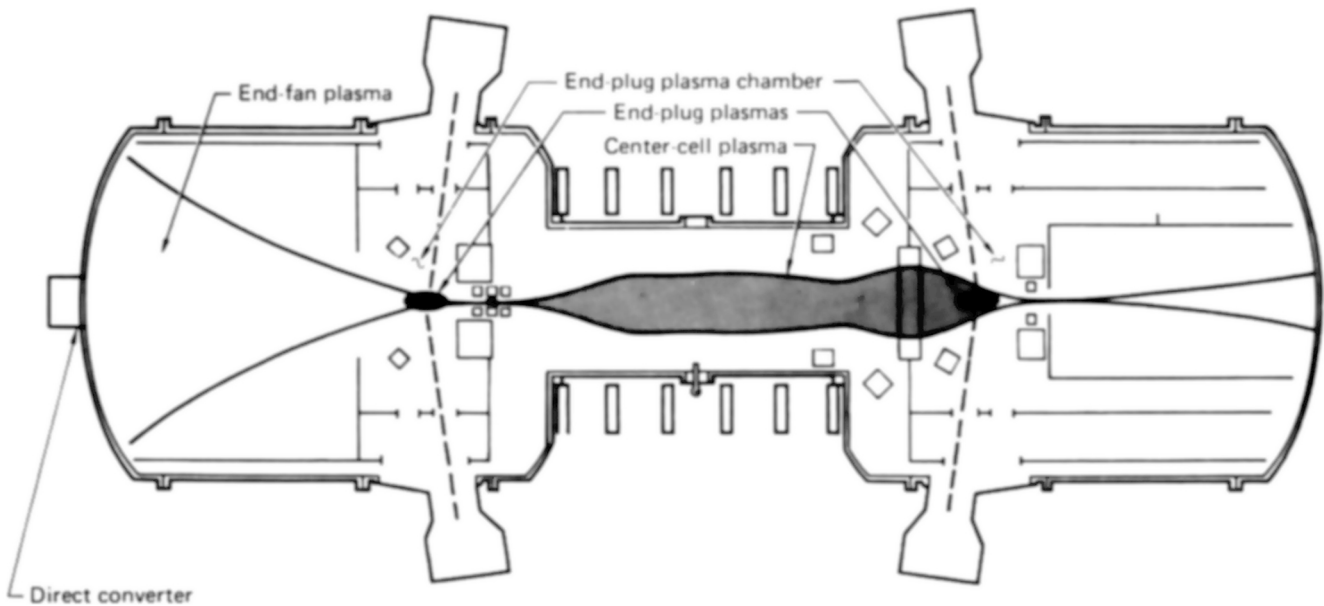


Fig. 13. Schematic of the TMX device showing the location of the direct converter module.

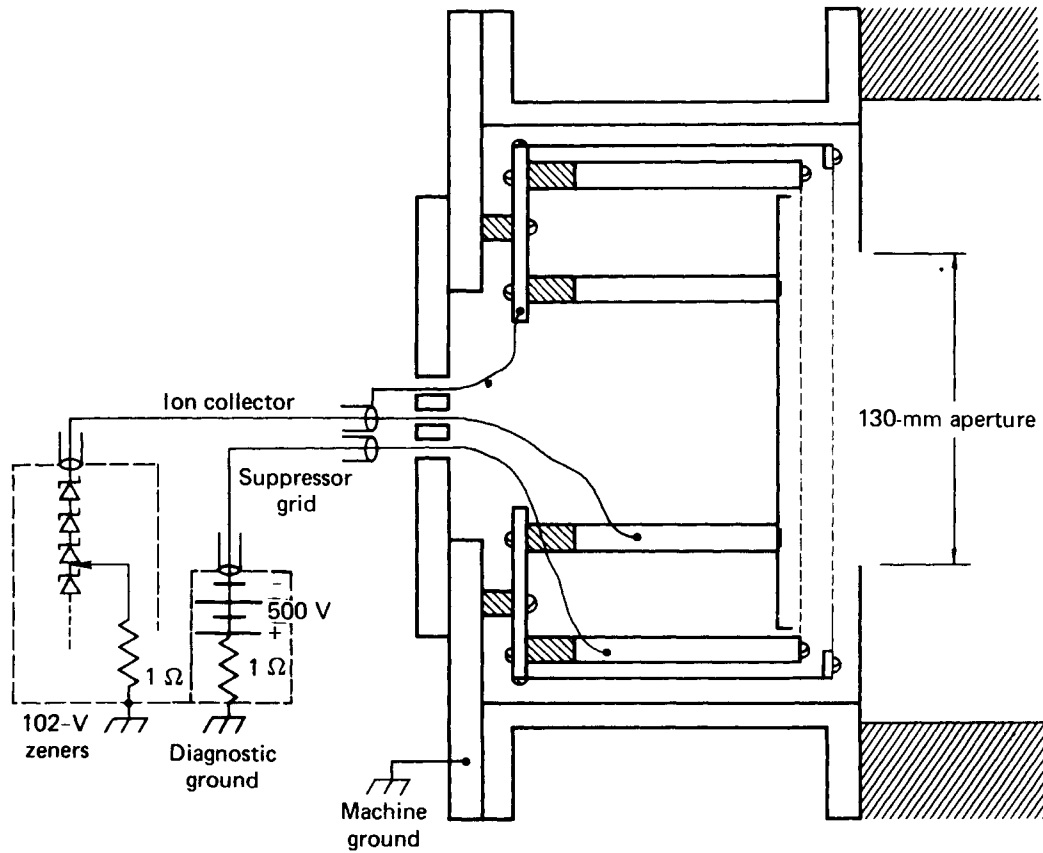


Fig. 14. Sketch of the single-stage direct converter that was tested on TMX. The collector voltage was developed across the string of zener diodes. A net power of 67 W was recovered for an efficiency of 48%.

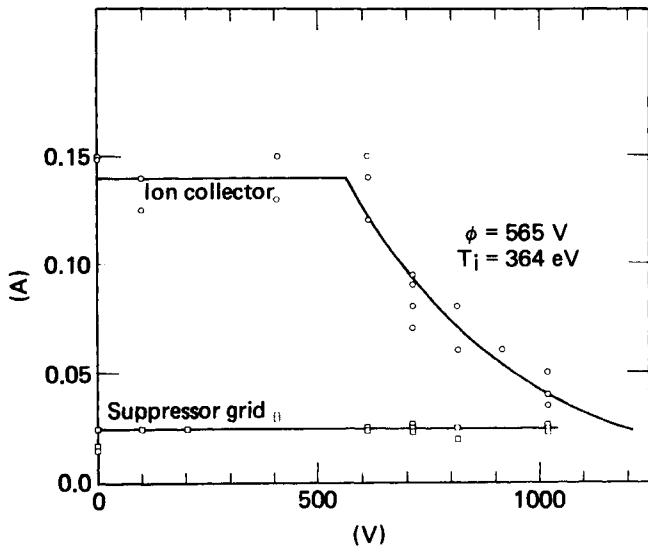


Fig. 15. Data from the single-stage direct converter tested on TMX. A net 0.14 A was collected when the collector potential was < 565 V, indicating the minimum ion energy.

gives T_i , the temperature of the confined ions. If the loss cone is not full, then the rate of decrease is distorted by the rate that ions of different energies scatter into the loss cone. In either case, the magnetic expansion before the ions reach the PDC has little effect because the loss cone includes only those ions with small pitch angle.

Figure 15 shows that 0.14 A can be collected at 565 ± 20 V, while the drain at the suppressor grid is 0.025 A at -500 V. The net recovered power is then 67 W, while the incident ion power is ~ 140 W (0.15 A of ions with an average energy of 930 eV). The measured value of efficiency of the PDC is, therefore:

$$\eta = 67 \text{ W} / 140 \text{ W} = 0.48 \pm 0.02 .$$

We can calculate the efficiency using Eqs. (1) and (2). At this low energy, $\sigma_i \approx \sigma_{cx} \approx 0$, $r^+ = 0$, and $T_g = 0.97$. Therefore, Eq. (1) gives: $I_g = (0.032I)(1 + \gamma_1 + 0.97r^0\gamma_c)$, while Eq. (2) gives: $I_1 = 0.934I - (0.032I)(1 + 0.97r^0\gamma_c)$, since $f \approx 0.5$ here. If we assume the values $\gamma_1 \approx \gamma_c \approx 2$ and $r^0 \approx 0.3$, we find $I_g \approx 0.12I$, and $I_1 \approx 0.88I$. With $V_1 = 565$ V,

$V_g = 500$ V, and $W = 930$ eV, Eq. (3) then predicts an efficiency of:

$$\eta = \frac{0.88I \times 565 - 0.12I \times 500}{I \times 930} = 0.47 .$$

The calculated efficiency of 47% agrees well with the measured efficiency of $48 \pm 2\%$.

X. CONCLUSIONS

The high-power, single-stage PDC was operated for a total of ~ 78 h, mostly with 100-keV ions. No unexpected problems (such as sparking or deterioration at the grids) were detectable. The measured efficiency agrees with predictions to within the uncertainty in the parameters (secondary electron emission coefficients, cross sections, and reflection coefficients). With the two-stage, venetian-blind PDC, an unexpected problem arose due to the secondary electrons produced by ions that are reflected as fast neutrals from the ribbons. This problem should not arise in a full-scale PDC where the support structure is well removed from the beam. The successful test of a PDC module on the TMX machine lends confidence in our designs and scaling laws.

Before a full-scale PDC can be designed with confidence, we need experience with voltage holding. The large surface areas in a full-scale PDC will result in a large amount of capacitively stored electrical energy that could cause serious damage in the event of a spark.

NOMENCLATURE

a	= grid wire spacing
d_0	= spacing between the grid planes (defined in Fig. 2)
d_1	= spacing between suppressor grid and ion collector
d_2	= electrode spacing
E_r	= average electric field at the surface of a wire in the suppressor grid (kV/cm)
E_1	= electric field (kV/cm)
E_2	= electric field (kV/cm)
$f = f(V_1)$	= fraction of secondary electrons released from the suppressor grid that reach the ion collector when the grid is bombarded from both sides
h	= venetian-blind ribbon separation distance (cm)

I	= incident ion beam current (A)
I_g	= suppressor grid current (A)
I_{rg}	= ribbon suppressor grid current (A)
I_{sh}	= grid mount and shield current (A)
I_1	= net positive current from the ion collector I_1 (A)
I_2	= net positive current from the ion collector I_2 (A)
l	= ribbon width (cm)
n_0	= gas density (cm^{-3})
p	= gas pressure (mPa or Torr)
R	= variable load resistor (Ω)
r	= grid wire radius (mm)
$r_{1,2}^+$	= coefficient for the electrostatic reflection of an ion back from a metal surface
$r_{1,2}^0$	= coefficient for the reflection of an ion back from a surface as a fast neutral atom
R_{th}	= nonlinear resistor (Ω)
$S_{cx}(a,b)$	= integral of σ_{cx} from a to b , taking into account ion energy variation (cm^3)
$S_i(a,b)$	= integral of σ_i from a to b , taking into account ion energy variation (cm^3)
$T_f = T_f(V_1, W)$	= forward transmission of ions of energy W
T_g, T_{rg}	= grid transparency
T_r	= ribbon transparency for product ions and electrons
V_g	= grid voltage (kV)
$V_{1,2}$	= collector voltage (kV)
W	= initial incident ion energy (kV)
\bar{x}	= distance to zero in potential defined in Fig. 2 (cm)
α_0	= incident angle at first grid (deg)
α_1	= ribbon slope angle
γ_1	= coefficient for the production of secondary electrons by a primary ion
γ_c	= coefficient for the production of secondary electrons by cold ions

- σ_{cx} = cross section for the charge exchange of a beam ion with a gas molecule (cm^2)
- σ_i = cross section for the production of electrons by collision of beam ions with gas molecules (cm^2)

ACKNOWLEDGMENTS

We gratefully acknowledge the technical support of J. D. Kinney and M. C. Fowler.

This work was performed under the auspices of the U.S. Department of Energy by LLNL under contract W-7405-eng-48.

REFERENCES

1. R. F. POST, "Mirror Systems: Fuel Cycles, Loss Reduction and Energy Recovery," *Proc. BNES Nuclear Fusion Reactor Conf.*, Abingdon, England, September 1969, p. 88 (1969).
2. W. L. BARR and R. W. MOIR, "A Review of Direct Energy Conversion for Fusion Reactors," *Proc. 2nd Topl. Mtg. Technology of Controlled Nuclear Fusion*, Richland, Washington, September 21-23, 1976, CONF-760935, Vol. IV, p. 1181 (1976).
3. R. W. MOIR and W. L. BARR, "'Venetian Blind' Direct Energy Converter for Fusion Reactors," *Nucl. Fusion*, **13**, 35 (1973).
4. W. L. BARR, R. W. MOIR, and G. W. HAMILTON, "Test Results on a High-Power, 100-keV Beam Direct Converter," *J. Fusion Energy*, **2**, 131 (1982).
5. T. K. FOWLER and B. G. LOGAN, "The Tandem Mirror Reactor," *Comments Plasma Phys.*, **2**, 167 (1977); see also G. I. DIMOV, V. V. ZAKAIDAKOV, and M. E. KISHINEVSKY, "Open Trap with Ambipolar Mirrors," *Fiz. Plasmy*, **2**, 597 (1976).
6. K. R. SPANGENBURG, *Vacuum Tubes*, McGraw-Hill Book Company, New York (1948).
7. H. VERBEEK, *Radiation Effects on Solid Surfaces*, Chap. 10, M. KAMINSKY, Ed., American Physical Society (1976); see also O. C. OEN and M. T. ROBINSON, *Nucl. Instrum. Methods*, **132**, 647 (1976).
8. G. A. CARLSON, B. ARFIN, W. L. BARR, B. M. BOGHOSIAN, J. L. ERICKSON, J. H. FINK, G. W. HAMILTON, B. G. LOGAN, J. O. MYALL, and W. S. NEFF, Jr., "Tandem Mirror Reactor with Thermal Barriers," UCRL-52836, Lawrence Livermore National Laboratory (Sep. 1979).
9. C. F. BARNETT et al., "Atomic Data for Controlled Fusion Research," ORNL-5206, Vol. 1, Oak Ridge National Laboratory (1978).
10. F. H. COENSGEN et al., "Electrostatic Plasma Confinement Experiments in a Tandem Mirror System," *Phys. Rev. Lett.*, **44**, 1132 (1980).
11. P. COAKLEY, J. F. CLAUSER, and N. HERSHKOWITZ, "Collecting and Emitting Langmuir Probe Measurements at the End Wall of TMX," *Bull. Am. Phys. Soc.*, **25**, 879 (1980).